Solar Synthesis of PbS−SnS_2 Superstructure Nanoparticles

Olga Brontvein,[†] Ana Albu-Yaron,[†] Moshe Levy,[†] Daniel Feuerman,[‡] Ronit Popovitz-Biro,[§] Reshef Tenne,[†] Andrey Enyashin,*[,∥] and Jeffrey M. Gordon*[,‡]

[†]Department of Materials and Interfaces, Weizmann Institute of Science, P.O. Box 26, Rehovot 76100, Israel, [‡]Department of Solar Energy and Environmental Physics, Jacob Blaustein Institutes for Desert Research, Ben-Gurion University of the Negev, Sede Boqer Campus, Sede Boqer 84990, Israel, [§]Electron Microscopy Unit, Weizmann Institute of Science, P.O. Box 26, Rehovot 76100, Israel, and [∥]Institute of Mathematics and Computer Sciences, Ural Federal University, Lenina Pr. 51, Ekaterinburg 620000, Russia

ABSTRACT We report the synthesis and supporting density-functional-theory computations for a closed-cage, misfit layered-compound superstructure from PbS−SnS_2, generated by highly concentrated sunlight from a precursor mixture of Pb, SnS_2, and graphite. The unique reactor conditions created in our solar furnace are found to be particularly conducive to the formation of these nanomaterials. Detailed structural and chemical characterization revealed a spontaneous *inside-out* formation mechanism, with a broad range of nonhollow fullerene-like structures starting at a diameter of ∼20 nm and a wall thickness of ∼5 layers. The computations also reveal a counterintuitive charge transfer pathway from the SnS_2 layers to the PbS layers, which indicates that, in contrast to binary-layered compounds where it is principally van der Waals forces that hold the layers together, polar forces appear to be as important in stabilizing superstructures of misfit layered compounds.

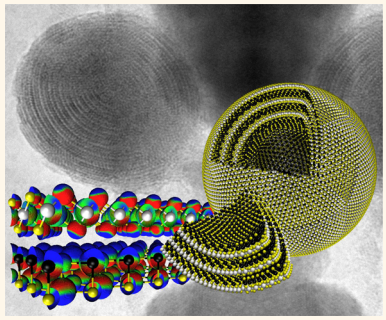

KEYWORDS: fullerene-like · inorganic · misfit layered compound · superstructure · PbS · SnS_2 · density functional theory · solar · charge transfer

Transition metal dichalcogenide compounds (*e.g.*, MoS_2, $MoSe_2$, WS_2, WSe_2, NbS_2 and $NbSe_2$, to name just a few) crystallize in a layered structure analogous to that of carbon or hexagonal BN. Because the dangling bonds on the rim of the layers are chemically reactive, folding of the layers and seaming of the edges can result in the formation of hollow closed-cage nanostructures:[1,2] inorganic fullerene-like (IF) structures and inorganic nanotubes (INT). Typically, high temperatures are needed to render the two-dimensional (2D) nanosheets flexible enough to fold and form seamless closed-cage nanostructures.[3] The hollow core of such nanostructures (2−10 nm in diameter) is appreciably larger than the stability range of the chemical bonds (<0.5 nm), and the S or Se atoms that decorate the hollow core are fully bonded and hence nonreactive.

The Sn−S system[4] is the starting point for our consideration of misfit layered nanostructures, and hence for motivating the current investigation. Sn−S compounds can form a layered structure in two stable forms: (1) α-SnS (herzenbergite) has a GeS structure with an orthorhombic (pseudotetragonal highly distorted NaCl) unit cell (a = 1.118, b = 0.398, c = 0.432 nm; *Pnma*),[5] and (2) α-SnS_2 has a CdI_2 layered (trigonal-1T) structure with a pseudohexagonal unit cell (a = 0.36486 and c = 0.58992 nm).[6] Both the synthesis of closed-cage SnS_2 nanoparticles[7] and computational studies of SnS_2 nanotubes[8] have been reported. More recently, IF and INT SnS_2 were synthesized by a vapor transport technique in a single-step 2 h process, using bulk Sn grains and CS_2 in a furnace at 850 °C under Ar or an Ar/CS_2 mixture.[9]

Laser ablation of SnS_2 resulted in a loss of sulfur and the condensation of nanoparticles of the mixed SnS−SnS_2 phase as fullerene-like structures and short nanotubes.[10] Careful analysis of the nanostructures suggested that they comprise a misfit layered compound (MLC) consisting of sequential layers (superstructure) of SnS and SnS_2 with different periodicities.

MLCs consisting of alternating mono (MS, denoted by O) and disulfide (TS_2, denoted by T) layers have previously been investigated in depth.[11,12] The lattice mismatch

* Address correspondence to jeff@bgu.ac.il, enyashin@ihim.uran.ru.

Received for review April 22, 2015 and accepted July 8, 2015.

Published online July 08, 2015
10.1021/acsnano.5b02412

between the two alternating layers leads to intrinsic stress in the superstructures, which can be partially relaxed by bending, folding and forming tubules.[13,14] This constitutes an additional mechanism for the closure of such nanostructures.[15] Namely, the propensity of MLCs to form closed-cage hollow nanostructures stems from the relaxation of the mismatch between the two sublattices (in addition to the recognized contribution of the saturation of dangling bonds at the rim).[16]

Nanotubes of misfit compounds were previously synthesized using conventional ovens at temperatures <1000 °C, formed by the folding of molecular slabs along one direction only. Our solar furnace (Figure 7 in the Methods section below) produces target temperatures in excess of 2000 °C, at which the difference in the coefficient of thermal expansion of the two sublattices (PbS and SnS_2) induces an excess strain that can be partially relaxed by forcing the PbS−SnS_2 superstructure to fold along two axes, thereby forming a quasi-spherical fullerene-like nanoparticle. Furthermore, the large temperature gradients in the reactor endow extra flexibility to the folding superstructure, allowing it to adopt small radii of curvature. The combination of these distinct driving forces leads to the formation of the unique small-radius fullerene-like nanoparticles observed in this study.

Because PbS and SnS_2 are semiconductors with different bandgaps (0.41 and 2.44 eV, respectively, at room temperature),[17,18] the misfit PbS−SnS_2 nanostructures are expected to reveal interesting optical absorption in the visible range, which could spawn applications in photocatalysis and photodetection. It remains to be seen whether the optical properties of the two components of the misfit nanoparticles amalgamate into a single absorption edge, or preserve the separate absorption thresholds of the two components. This notion is not limited to electronic excitations, and could also pertain to properties such as vibronic states.

Recently, a computational investigation of the structural, energetic and electronic properties of SnS and SnS_2 predicted the properties of the monolayers of each of the compounds in the SnS−SnS_2 double layer system and of the nanotubes of the misfit structure, and were found to be in good agreement with experimental measurements.[19,20] In many MLCs, charge transfer from the distorted rock-salt (MS) layer to the hexagonal TS_2 layer is believed to occur.[21] However, counter to this intuitive picture, the calculations[20] showed a small but definite electron transfer from the SnS_2 layer to the SnS layer. Thus, in contrast to binary-layered compounds, where van der Waals forces play the major role in holding the layers together, polar forces seem to play an equally important role in stabilizing MLC superstructures.

Here, we report experiments in which highly concentrated sunlight irradiated a mixed powder of Pb, SnS_2 and graphite to induce a high-temperature solid-state reaction that yielded unprecedented IF nanostructures of PbS−SnS_2 MLC, with fairly reproducible yields up to ~10% (elaborated in the Methods section below). The stability of these MLC nanostructures is corroborated by detailed *ab initio* calculations. Furthermore, a small but definite charge transfer from the SnS_2 layer to the PbS layer can be deduced, analogous to a previous study on anomalous interlayer charge transfer in MLC SnS−SnS_2.[19]

RESULTS AND DISCUSSION

The fullerene-like PbS−SnS_2 superstructures we observed constitute a distinct type of misfit structure. In the bulk, PbS (*Fm*3*m*) exhibits a rock-salt structure with a lattice parameter of 0.5934 nm.[22] However, upon stacking with SnS_2 ($P\bar{3}m$)[6] layers, this structure is modified into a PbS (*Cm*2*a*)[13] layered structure.

Figure 1 displays the SEM (a), low-magnification (b) and high-magnification (c) TEM images of the observed PbS−SnS_2 superstructures, plus a profile showing a *d*-spacing of 1.188 nm, corresponding to the MLC PbS−SnS_2 (which, according to the literature,[13,22] should be 0.587 + 0.590 = 1.177 nm). The diameter of these superstructures varied from 20 to 300 nm.

A PbS−SnS_2 superstructure with O−T sequential order can be seen in the high-resolution STEM HAADF image of a single nanoparticle (Figure 2a), where the contrast is proportional to atomic number (*Z*), and the brightness of both layers appears almost the same.

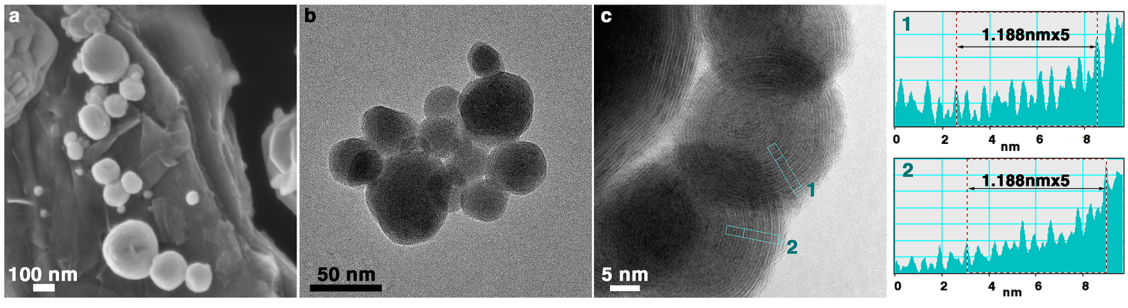

Figure 1. SEM (a), low-magnification TEM (b), and high-magnification TEM (c) images of PbS−SnS_2 superstructures. A profile showing a *d*-spacing corresponding to the PbS−SnS_2 misfit compound is also included.

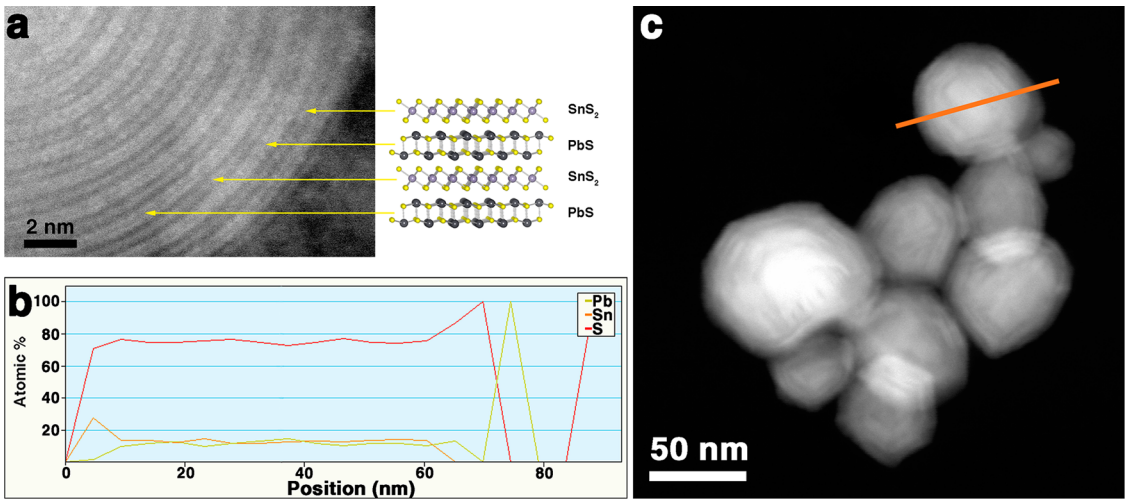

Figure 2. (a) High-resolution STEM HAADF image of a single PbS−SnS_2 superstructure. (b) Line scan STEM EDS profile of a single nanoparticle along the line in (c). (c) STEM HAADF image of PbS−SnS_2 superstructures.

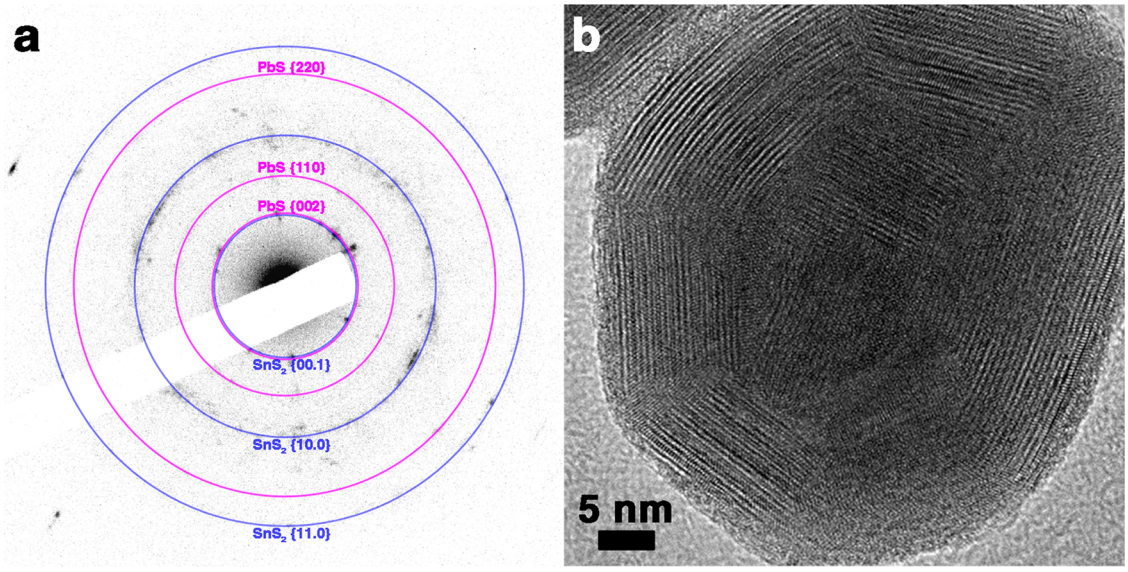

Figure 3. (a) Selected area electron diffraction of a single PbS−SnS_2 nanoparticle. Blue circles belong to the SnS_2 structure, and magenta circles belong to the PbS structure. The inner circle corresponds to the interlayer distance of 5.9 nm and is common to both structures. (b) The corresponding TEM image.

Although Pb is heavier than Sn, the Sn layers contain only Sn atoms, whereas each Pb layer contains a mixture of Pb and S atoms (such that the layer's average atomic weight is smaller than for pure Pb). This observation supports the interpretation that the superstructure is constructed from alternating PbS−SnS_2 layers with the O−T sequence. Further supporting evidence for this conclusion follows from the STEM EDS analysis, where the line scan profile of a single nanoparticle (Figure 2b) shows a 1:1 ratio between Pb and Sn, corresponding to the suggested (O−T) superstructure for the MLC PbS−SnS_2.

From the selected area electron diffraction pattern of a single nanoparticle, two sets of dots (marked by circles) that belong to SnS_2 and PbS structures are evident (Figure 3). The blue and magenta circles belong to the SnS_2 and PbS structures, respectively. The inner circle is common to both structures, and corresponds to the interlayer separation of 5.9 nm.

The PbS−SnS_2 IF superstructures can be divided into two types, depending on their size. The relatively small (<50 nm) nanoparticles have an almost perfect spherical shape (Figure 4a), while the larger nanoparticles exhibit faceted (Figure 4b) structures formed around a PbS−SnS_2 slab.

In all cases, the cores of these superstructures were not hollow, suggesting formation by an *inside-out* mechanism, which commonly follows from fast nucleation and growth, as in the synthesis of IF−TiS_2 nanoparticles from $TiCl_4$ and H_2S.[23] The size of the PbS−SnS_2 nanoparticles is self-limited, dictated by their stability limit and nucleation rate. This contrasts with the more

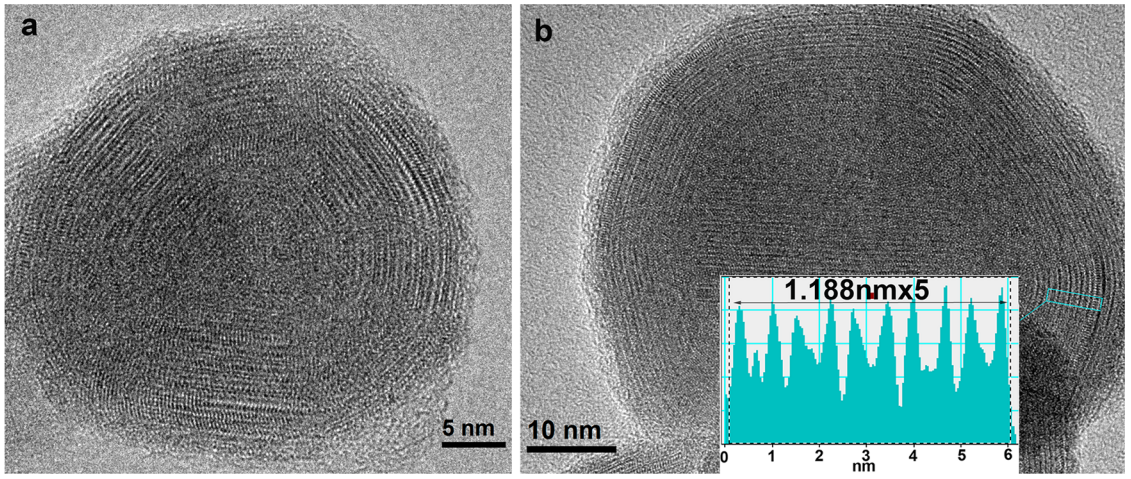

Figure 4. TEM images of IF−PbS−SnS_2 superstructures. (a) Small spherical nanoparticle. (b) Nanoparticle formed around a PbS−SnS_2 slab. The inset intensity profile (in blue in the framed rectangle) confirms the *d*-spacing of the misfit PbS−SnS_2.

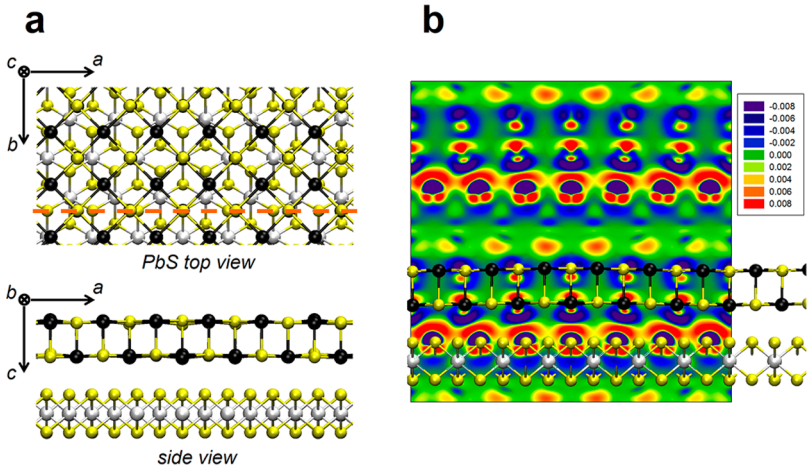

Figure 5. (a) Stick-and-ball model of the optimized unit cell of the bulk PbS−SnS_2 misfit lattice (Pb, Sn, and S atoms are in black, gray, and yellow, respectively). The dashed red line represents the cut plane used for the calculation of the Mulliken charge distribution illustrated in (b). (b) Results of the DFT GGA calculations. The computed charge redistribution is within the "a−c" cross section marked in (a) by a red dashed line. The increase and decrease of charge density, in $|e|/Å^3$, are colored blue and red, respectively.

common *outside-in* growth of IF nanoparticles,[2,24] where, for example, incipient metal−oxide (or amorphous metal−sulfide) nanoparticles first nucleate and only subsequently are converted into IF−WS_2 (IF−MoS_2) *via* a high-temperature, diffusion-controlled reaction.

Computation of Superstructures, Nanoparticle Stability, and Charge Transfer. *Ab Initio Calculations. PbS−SnS_2 Misfit Superstructures.* Numerous misfit structures are possible for PbS−SnS_2 depending on their chemical composition, the stacking order of the layers, and the relative orientation of the PbS and SnS_2 layers (in the *a*−*b* plane). Taking into account the associated time-intensive analysis with DFT, we adopted the simplest misfit structure of stacked alternating molecular sheets of PbS and SnS_2. Preliminary detailed DFT calculations of the bulk, and of nanocrystals only a few layers thick, confirmed that adequate accuracy is then achieved for modeling the crystalline structure and electronic states. The unit misfit PbS−SnS_2 cell was then designed as the smallest one possible for rectangular symmetry, which implies a commensuration between the 7 × 2 supercell of a SnS_2 single layer in its $a \times \sqrt{3}a$ (orthopseudohexagonal) representation and the 6 × 3 supercell of a PbS layer in its $a/\sqrt{2} \times a/\sqrt{2}$ representation (Figure 5a). Thus, the composition of the unit cell can be described as $(PbS)_{36}(SnS_2)_{28}$, *i.e.*, $(PbS)_{1.286}SnS_2$, which engenders a respective mismatch of 1.5% and 2.6% in the *a* and *b* directions. The initial value of the lattice parameter *c* for the misfit unit cell was chosen as the sum of *c* and *a*, optimized for SnS_2 and PbS, respectively.

A full-geometry optimization of the PbS−SnS_2 misfit reveals a slight expansion of the initial model in all directions, with lattice parameters a = 25.78 Å and b = 12.77 Å, which are close to their corresponding values in bulk 1T-SnS_2 ($P\bar{3}m1$) and fcc-PbS ($Fm\bar{3}m$) compounds. The *c*-axis (c = 12.11 Å) of the relaxed misfit PbS−SnS_2 structure is also larger than its initial value of 11.73 Å

TABLE 1. Calculated Lattice Parameters (a_i, b_i), Interlayer Distances (w), Young's Moduli (Y), Poisson Ratios (ν), and Interface Energies (σ) of Different PbS and SnS_2 Layers, Estimated Using DFT-GGA Calculations[a]

	ν_i	Y_i, GPa	Y_i, eV/Å^2	w_i, Å	a_i, Å (b_i, Å)
SnS_2 layer	0.3568	158[c]	0.9882	5.73[b]	3.71
PbS layer	0.3052	165	1.0310	5.79	5.97
Bulk PbS−SnS_2	-	-	-	12.11	25.78 (12.77)
Bulk SnS_2	-	-	-	-	3.74
Bulk PbS	-	-	-	-	6.01

σ(PbS−SnS_2) = −24.8 meV/Å^2

[a] These parameters were also used for the phenomenological model to evaluate the stability of the misfit PbS−SnS_2 fullerene-like nanoparticles. [b] This distance is also equivalent to the lattice parameter c of bulk 1T-SnS_2. [c] This value changes to 163 GPa in the *zigzag* direction, and 154 GPa in the *armchair* direction.

(which is the arithmetic mean of the interlayer distances of pure SnS_2 and PbS). There is an increase of the interplane distances in the c direction for both the SnS_2 and PbS molecular sheets. The distance between the sulfur planes within the SnS_2 layer is increased to 3.07 Å, from its bulk value of 3.02 Å. A corrugation of the PbS layer within the misfit is also visible. The distance between sulfur planes within the two PbS layers varies from 2.36 Å (bulk) to 2.96 Å in different parts of the unit cell. Such changes in the structure provide evidence that the interaction between the SnS_2 and PbS molecular slabs does not have a simple van der Waals character. Table 1 summarizes the structural computations.

Charge Transfer within the PbS−SnS_2 Slab. Calculating the interface energies within the misfit superstructures and the corresponding parent bulk phases revealed putatively surprising (nonintuitive) results for charge transfer *from* the SnS_2 layers *to* the PbS layers within the interface. Figure 5b demonstrates the in-plane charge redistribution at the middle of the van der Waals gap of the misfit PbS−SnS_2 (decreases and increases of electron density, in $|e|$/Å^3, are colored red and blue, respectively). A Mulliken charge distribution analysis shows that the SnS_2 slab donates around 3.24 e, and the PbS slab accepts 2.96 e, per unit cell of the misfit structure. The rest of the electrons increase the electronic density within the van der Waals gap (Figure 5a). This corresponds to the transfer of 0.12 e per SnS_2 stoichiometric unit. These findings are deemed counterintuitive insofar as charge transfer would be expected *from* the slab containing the metal in a reduced state (Pb) *to* that with the higher valence (Sn). Charge transfer of a similar magnitude (0.1 e) had been reported earlier in the SnS−SnS_2 misfit structure, *from* the SnS_2 *to* the SnS unit.[19]

Our computation of the cohesion energy between the SnS_2 layers within 1T-SnS_2, and between the PbS molecular sheets within fcc-PbS, yielded 15 and 18 meV/Å^2, respectively, consistent with computed estimates for the surface energies of bulk PbS,[32] as well as with calculated values for other layered dichalcogenides.[33,34] (We are unaware of corresponding data or estimates for SnS_2.) However, the calculated cohesion between PbS and SnS_2 layers *within* the misfit PbS−SnS_2 layer is found to be stronger: 25 meV/Å^2 (Table 1). The discrepancy between these values implies that the relative stability of these nanostructures may be different from those of layered compounds with pure van der Waals interactions between layers (*vide infra*).

Stability of the PbS−SnS_2 Fullerene-like Nanoparticles. Because our misfit PbS−SnS_2 fullerene-like particles comprise thousands of atoms, a direct systematic investigation of their stability by means of quantum mechanical calculations is prohibitively time-intensive. Therefore, only a phenomenological model was attempted. Related models have been used to predict the relative stability of different MoS_2 nanostructures.[35]

The exact nature, number, and distribution of the defects causing the sphericity of the observed multiwalled misfit nanoparticles have not yet been established. As a first approximation, we assumed that the number of possible defects should be small compared to the total number of atoms. Thus, the excess particle energy ΔE (compared to a flat single slab of SnS_2 or PbS) can be estimated as the sum of the strain energy of the curved layers and the interface energy between concentric spherical walls.

From elasticity theory, ΔE per surface area (S) of an individual single-wall particle of radius R can be estimated as the energy of the mechanical stress of a layer bent into a sphere:

$$\frac{\Delta E}{S} = \frac{1+\nu}{12}\frac{Yw^3}{R^2} \quad (1)$$

where w, Y, and ν are the thickness, Young's modulus, and Poisson ratio of the corresponding flat layer, respectively.

Taking into account the interface energy σ due to van der Waals interactions and the charge transfer between the layers, eq 1 can be extended to a general k-walled hollow spherical nanoparticle:

$$\frac{\Delta E}{S} = \frac{1/12\sum_{i=1}^{k}(1+\nu_i)Y_i w_i^3 + \sum_{i=1}^{k-1}\sigma_{i,i+1}R_i^2}{\sum_{i=1}^{k}R_i^2} \quad (2)$$

where σ can assume 1 of 3 values depending on the PbS−SnS_2 interface, and the values of w, Y, ν, and σ depend on the nature of a particular PbS−SnS_2 sheet. All these parameters were calculated with the same DFT methodology noted above for the SnS_2 monolayer, the PbS layers consisting of 2 atomic planes, the bulk compounds PbS and SnS_2, and the misfit PbS−SnS_2 (Table 1).

Figure 6 illustrates the dependence of the excess energy on diameter D for hollow spherical PbS−SnS_2

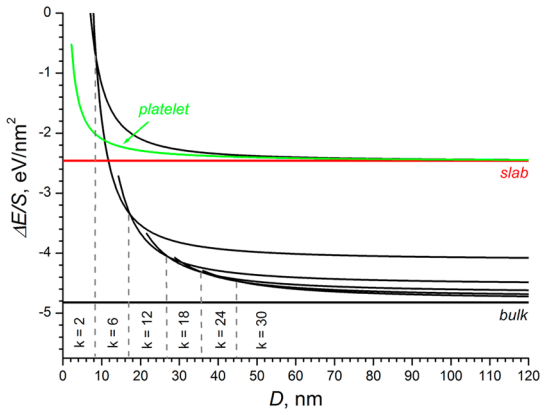

Figure 6. Energies per surface area $\Delta E/S$ of the multilayered spherical fullerene-like PbS−SnS_2 hollow nanoparticles as a function of their diameter D. The vertical dashed lines delimit regions where indicated values of k are most stable. (All possible values of k are not indicated in the spirit of clarity of presentation.) For comparison, the energies for the disk-shaped nanoplatelets, the single slab, and the bulk PbS−SnS_2 misfit are also plotted. The curve labeled "slab" refers to an infinite PbS−SnS_2 monolayer.

misfit nanoparticles, for several values of the total number k of alternating PbS and SnS_2 layers. The energies follow a roughly $1/D^2$ behavior over the entire range of diameters, and approach the values of the corresponding planar layers.

At small nanoparticle sizes, the strain energy contribution to the excess energy should become comparable to the energy of the highly reactive edges that form after the particles burst and exfoliate. Thus, a comparison of the energies of fullerene-like particles and flat PbS−SnS_2 nanoplatelets or nanoflakes sheds light on their minimal possible size. The energy of a disk-shaped platelet of radius R_{pi} is roughly proportional to $2\pi R_{pi}\varepsilon_{di}$, where ε_{di} is the average energy of the dangling bonds at the edges of a SnS_2 or PbS nanoplatelet. DFT estimates of ε_{di} for sample stoichiometric edges of (4,0)SnS_2 and (3,0)PbS nanostripes yielded $\varepsilon_d(SnS_2)$ = 34.2 meV/Å and ε_d(PbS) = 26.9 meV/Å. The corresponding results are plotted in Figure 6, where it can be seen that double-walled fullerene-like PbS−SnS_2 particles are less stable than the nanoplatelets at any size, and should therefore tend to undergo self-exfoliation. However, a stabilization of the spherical morphology can be observed for multiwalled particles at diameters exceeding 10 nm. (A derivation of the corresponding equations for the larger, faceted nanoparticles, and evaluation of nanoparticle stability, would require establishing how the bending energy of each layer varies with bending angle, requiring inordinately long computer times even for a single misfit layer, and hence are not included here.)

In Figure 6, the dashed vertical lines delimit domains where selected values of k are most stable. For example, k = 2 is most stable at D < 10 nm. A sharp increase in stability appears at k = 6. For D > 30 nm and k > 18, the curves become essentially indistinguishable and have numerous intersections. These findings suggest that nanoparticles covering a wide size distribution and with a large wall thickness should be observed—predictions in agreement with the present experimental results.

Insights into the Growth Mechanism of Closed-Cage Nanostructures from Misfit Compounds. *The Driving Forces.* The driving force of the misfit between two lattices plays a pivotal role in the folding of molecular layers, that in turn results in IF structures, above and beyond the established closure mechanism of the saturation of dangling bonds at the periphery of common layered-type nanostructures. Recall that the two principal interactions in two-dimensional (2D, layered) nanomaterials are the strong chemical (mostly covalent) bonds within the molecular sheet, and the weak van der Waals interactions between the sheets, responsible for the stacking of the layers. Additionally, due to differences in the work functions of the two layers in the misfit structure, charge transfer may lead to stronger polarization forces. However, it is the large anisotropy between the *intra*- and *inter*-layer forces that dictates the 2D layered-type nature of the misfit compounds. The weak interlayer interaction grows insubstantial at high temperatures where thermal fluctuations enhance the bending, shearing, and folding of the molecular sheets and hence the formation of closed-cage nanostructures.

Suitability of the Experimental Configuration. In our solar ablation experiments, combining SnS_2, Pb, and graphite led to the spontaneous formation of IF nanoparticles of the misfit compound PbS−SnS_2, a nanostructure not previously reported or predicted. Because solar ablation is continuous, with a high *averaged* radiative power, the degree of heating of the *total* sample and its annealing environment is appreciably higher than for pulsed laser ablation. However, these conditions also create the undesired potential for oxidation of the precursor material by residual water and hydroxyl moieties adsorbed to the ampule's inner surface. Graphite was added to the reaction mixture to mitigate this contingency. Nonetheless, the highly reducing carbon vapors may influence the chemistry occurring in the ampule during irradiation. (Carbon *vapors* are posited because earlier experiments in essentially the same solar furnace generated peak temperatures that sublimed graphite.)

Nanostructure Features and Their Ramifications. Two striking features of the observed products are (a) the observation of closed-cage nanoparticles of very small diameter (<30 nm), and (b) the small-to-vanishing core diameter, which have several consequences:

1. The reaction occurs in a kinetically controlled *inside-out* mechanism, where each of the observed IF nanoparticles likely forms by condensation from the gas phase. This mechanism is promoted by the high temperature (>2000 °C) and strong temperature

gradient in the reaction zone. Therefore, the fast cooling rate of the plume favors rapid nucleation and growth-type reactions. Figure 4b shows an IF nanoparticle which formed by nucleation on an incipient PbS−SnS_2 slab. Wrapping of the PbS−SnS_2 layers on an emerging core promotes such an *inside-out* growth mechanism.

2. Although the small-to-vanishing diameter of the core might appear to favor a spiral-type growth, the folded PbS−SnS_2 layers seem to be seamlessly connected, which suggests a layer-by-layer growth mode in an *inside-out* mechanism, a pathway that has been observed before for the growth of various IF nanoparticles from the gas phase.[23] The small diameter of the nanoparticles can be attributed to the high temperature of the condensation process and the relaxation of the mismatch strain between the two layers. The high temperatures in the reaction zone render the layers very flexible, allowing them to bend with small radii of curvature.

3. The relatively strong interaction between the layers, induced by the combination of van der Waals *and* polar forces, imparts extra stability to the PbS−SnS_2 slabs. On the one hand, interlayer forces increase the shear forces and hinder relaxation of the folding layers to accommodate small radii of curvature. However, the extra interlayer polar forces stabilize the multiwall nanostructures at high temperatures, which is a prerequisite for formation of the observed structures (Figure 6). The extra stability beyond 12 layers and diameters of 30−40 nm is not significant, and entails the type of self-limiting growth observed here.

CONCLUSIONS

We have reported the generation of a fundamentally distinct type of *misfit* nanostructure, closed-caged nanoparticles from PbS−SnS_2, that, to our knowledge, had neither been proposed nor synthesized previously. Structural and chemical analyses revealed that these nanoparticles comprise alternating PbS and SnS_2 layers that form a misfit superstructure with an O−T sequence, with the nanostructures exhibiting diameters from 20 to 100 nm. The unique reactor conditions created in our solar furnace, combining continuous high target temperatures, large irradiated areas, ultrahot extensive annealing regions, and strong gradients in the reaction region, have proven to be conducive to the synthesis of these unique misfit nanostructures.

These PbS−SnS_2 nanoparticles can be distinctly categorized depending on their size and morphology. The smaller nanoparticles are almost perfectly spherical. The larger ones form around a PbS−SnS_2 slab, with faceted surface contours. In all cases, the core of the nanoparticles is basically *not* hollow, which suggests that these superstructures were created by an *inside-out*, layer-by-layer growth mechanism that has previously been observed in the growth of other IF nanoparticles from the gas phase in spontaneous and rapid processes.

Precisely because these PbS−SnS_2 misfit superstructures had never been predicted or addressed theoretically, and in order to better understand the stability and charge transfer of PbS−SnS_2 misfit superstructures, we performed detailed *ab initio* DFT calculations. Would theory properly predict the experimental observations in terms of nanoparticle diameter and shell thickness? Indeed, the theoretical predictions that nanoparticles should cover a wide size distribution and a broad range of wall thickness, starting at a diameter of ∼20 nm and a wall thickness of ∼6 layers, are in agreement with the present experimental results.

In addition, a small but definite charge transfer from the SnS_2 layers to the PbS layers within the interface of the bulk PbS−SnS_2 misfit crystal emerges. This charge transfer is counterintuitive insofar as the charge is transferred from a metal atom in a higher valence state (SnS_2) to a metal atom in a lower valence state (PbS).

In contrast to the broad assortment of binary layered compounds from which nanostructures have been prepared to date, where van der Waals forces between molecular layers play a major role in maintaining the layered structure, polar forces between the SnS_2 and PbS molecular slabs seem to play an equally important role in stabilizing misfit layered compound superstructures. The nominal success of computational methods for predicting the range of observable metastable superstructures augurs well for future studies in which a rich spectrum of such misfit layered nanostructures could be identified with theoretical tools that prompt suitable experiments for their synthesis.

METHODS

The solar furnace we designed, assembled, and employed is shown in Figure 7, and constitutes a minor variation on a prior version of this concentrator system.[36] Peak target irradiance reaches ∼15 000 suns (15 W/mm^2), on a focal spot a few mm^2 in area, with peak reactor temperatures approaching ∼3000 K, generating extensive ultrahot annealing regions and reactor conditions far from equilibrium that are not otherwise easily attained. (For contrast, in conventional oven-enhanced reactors, annealing environment temperatures are limited to <1500 K.) Also, due to the large angular range of the concentrated solar radiation reaching the reactor, substantial temperature gradients (>10^3 K/cm) are realizable in the reactor, conducive to the formation of metastable nanostructures, as evidenced in previous studies.[36] In some of the experiments, a small vibrator agitated the ampules during irradiation, with the aim of preventing agglomeration of the nanoparticles. Each exposure lasted 10 min, a duration based on prior successful syntheses of a variety of IF and INT materials.[36]

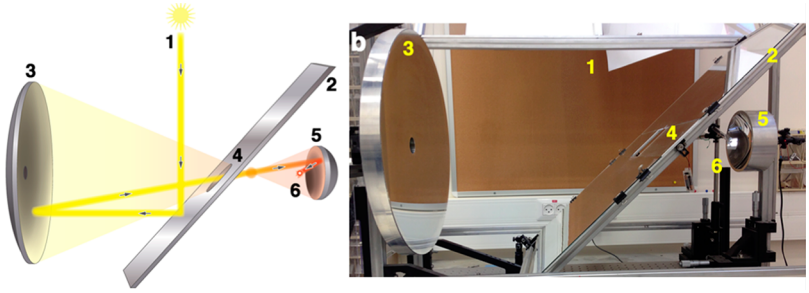

Figure 7. Schematic (a) and photograph (b) of our solar furnace. An outdoor dual-axis tracking flat mirror reflects solar beam radiation into an indoor lab. After a tilted flat mirror anchored in the ceiling directs the radiation downward (1), an additional tilted flat mirror (2) redirects the radiation parallel to the horizontal axis of a paraboloidal mirror (3) of diameter 526 mm and numerical aperture 0.40, that is confocal with the distal focus of a smaller ellipsoidal dish (5) of diameter 140.6 mm and numerical aperture 0.977, basically a Gregorian telescope. The reactor ampule is inserted into the proximate focus of the ellipsoid (6), where an irradiance of 15 000 suns (15 W/mm^2) is achieved during clear mid-day periods.

The reaction vessels were quartz (fused silica) ampules 250 mm in length and 14 mm in diameter. SnS_2 (>99.5%, Alfa Aesar), Pb (>99%, Strem), and graphite (>99%, <20 μm) powders were pulverized with an agate pestle and mortar. Each ampule was flushed by argon gas, then evacuated to 10^{-5} Torr, with the procedure being repeated several times before sealing approximately 220 mg of the precursor mixture in the ampule.

The nanoparticles were harvested mainly from the ampule wall, away from the irradiated region, with yields of the PbS–SnS_2 misfit layered compounds being ~10%. Other harvested products subsumed small quantities of PbS and Sn, along with the unreacted precursors Pb, SnS_2 and C. The reproducibility of experimental conditions was limited by (a) an accuracy of ~0.3 mm for manual positioning of the precursor powder in the ampule, within an irradiated focal spot area of several mm^2, (b) daily variations in solar beam radiation even for nominally clear-sky conditions, and (c) the ampule tilt of 30 ± 5° from the horizontal affecting not only the spatial distribution of the irradiated precursor, but also the location of the condensed products.

The graphite particles served two purposes: (1) high absorptivity across the solar spectrum, which facilitates the attainment of ultrahigh temperatures, and (2) as a high-temperature reducing agent for residual oxygen and moisture trapped in the ampules.

For characterization of the products, we used a JEOL Jem-2100 transmission electron microscope (TEM) operating at 200 kV, a Philips CM120 TEM operating at 120 kV, and a Carl Zeiss ULTRA 55 scanning electron microscope (SEM). Both TEM microscopes were equipped with an energy-dispersive X-ray spectroscopy (EDS) detector for chemical analysis (CM120 with EDAX Phoenix Microanalyzer; JEOL Jem-2100 with Thermo Scientific UltraDry EDS Detector). High-resolution imaging was achieved with an FEI Tecnai F30-UT with a field-emission gun operating at 300 kV. Line-scan EDS analysis was performed with an FEI Tecnai F20 scanning transmission electron microscope (STEM), operating at 200 kV, equipped with a high-angle annular dark field (HAADF) detector and EDS detector (EDAX-Phoenix Microanalyzer).

Computational Details. The calculations were performed using the SIESTA 2.0 implementation[25,26] of density-functional theory (DFT).[27] The exchange–correlation potential within the Generalized Gradient Approximation (GGA) with the Perdew–Burke–Ernzerhof parametrization were used.[28] The core electrons were treated within the frozen-core approximation, applying norm-conserving Troullier–Martins pseudopotentials.[29] The valence electrons were taken as $3s^23p^4$ for S, $5s^25p^2$ for Sn, and $6s^26p^2$ for Pb, while the $5d^{10}$ electrons of Pb were included in its semicore state. The pseudopotential core radii were chosen as 1.70 a_B for all S states, 2.98 a_B for all Sn states, 3.19 a_B for Pb 6s and Pb 6p, and 2.99 a_B for Pb 5d states (1 a_B = 0.529 Å). A double-ζ basis set was used throughout, along with a cutoff of 15 Å for *k*-point sampling[30] where the *k*-point mesh was generated by the method of Monkhorst and Pack.[31] The real-space grid used for the numeric integrations corresponded to an energy cutoff of 300 Ry. All calculations were performed using variable-cell and atomic-position relaxations, with convergence criteria corresponding to a maximum residual stress of 0.1 GPa for each component of the stress tensor, and a maximum residual force component of 0.01 eV/Å.

Conflict of Interest: The authors declare no competing financial interest.

Acknowledgment. A.E. acknowledges the Program for State Support of Leading Universities of the Russian Federation (Agreement No. 02.A03.21.0006 of August 27, 2013). This research was supported by Israel Science Foundation First Program Grant No. 469/11. We acknowledge the support of the Israel National Nano-Initiative, the H. Perlman Foundation, the Irving and Azelle Waltcher Foundations in honor of Prof. M. Levy, and the Irving and Cherna Moskowitz Center for Nano and Bio-Nano Imaging.

REFERENCES AND NOTES

1. Tenne, R.; Margulis, L.; Genut, M.; Hodes, G. Polyhedral and Cylindrical Structures of Tungsten Disulphide. *Nature* **1992**, *360*, 444–446.
2. Feldman, Y.; Wasserman, E.; Srolovitz, D.; Tenne, R. High-rate, Gas-Phase Growth of MoS_2 Nested Inorganic Fullerenes and Nanotubes. *Science* **1995**, *267*, 222–225.
3. Tahir, M. N.; Yella, A.; Sahoo, J. K.; Annal-Therese, H.; Zink, N.; Tremel, W. Synthesis and Functionalization of Chalcogenide Nanotubes. *Phys. Status Solidi B* **2010**, *247*, 2338–2363.
4. Sharma, R. C.; Chang, Y. A. The S-Sn (Sulfur-Tin) System. *Bull. Alloy Phase Diagrams* **1986**, *7*, 269–273.
5. Del Bucchia, S.; Jumas, J. C.; Maurin, M. Contribution a L'étude de Composés Sulfurés D'étain(II): Affinement de la Atructure de SnS. *Acta Crystallogr., Sect. B: Struct. Crystallogr. Cryst. Chem.* **1981**, *37*, 1903–1905.
6. Hazen, R. M.; Finger, L. W. The Crystal Structures and Compressibilities of Layer Minerals at High Pressure. I. SnS_2, Berndtite. *Am. Mineral.* **1978**, *63*, 289–292.
7. Parilla, P. A.; Dillon, A. C.; Parkinson, B. A.; Jones, K. M.; Alleman, J.; Riker, G.; Ginley, D. S.; Heben, M. J. Formation of Nanooctahedra in Molybdenum Disulfide and Molybdenum Diselenide Using Pulsed Laser Vaporization. *J. Phys. Chem. B* **2004**, *108*, 6197–6207.
8. Chang, H.; In, E.; Kong, K. J.; Lee, J. O.; Choi, Y.; Ryu, B. H. First-Principles Studies of SnS_2 Nanotubes: A Potential Semiconductor Nanowire. *J. Phys. Chem. B* **2005**, *109*, 30–32.
9. Yella, A.; Mugnaioli, E.; Therese, H. A.; Panthöfer, M.; Kolb, U.; Tremel, W. Synthesis of Fullerene- and Nanotube-Like SnS_2 Nanoparticles and Sn/S/Carbon Nanocomposites. *Chem. Mater.* **2009**, *21*, 2474–2481.
10. Hong, S.; Popovitz-Biro, R.; Prior, Y.; Tenne, R. Synthesis of SnS_2/SnS Fullerene-Like Nanoparticles: A Superlattice

With Polyhedral Shape. *J. Am. Chem. Soc.* **2003**, *125*, 10470–10474.
11. Wiegers, G. A.; Meerschaut, A. Structures of Misfit Layer Compounds $(MS)_nTS_2$ (M}Sn,Pb,Bi, Rare Earth Metals; T}Nb,Ta,Ti,V,Cr; 1.09 < n<1.23). *J. Alloys Compd.* **1992**, *178*, 351–368.
12. Rouxel, J.; Meerschaut, A. Misfit Layer Compounds $(MX)_n(TX_2)_m$ [M=Sn,Pb,Bi,Rare Earth; T=Transition Metal; X=S,Se; 1.08 < n<1.25; m=1,2]. *Mol. Cryst. Liq. Cryst. Sci. Technol., Sect. A* **1994**, *244*, 343–354.
13. Bernaerts, D.; Amelinckx, S.; Van Tendeloo, G.; Van Landuyt, J. Microstructure and Formation Mechanism of Cylindrical and Conical Scrolls of the Misfit Layer Compounds $PbNb_nS_{2n+1}$. *J. Cryst. Growth* **1997**, *172*, 433–439.
14. Gómez-Herrero, A.; Landa-Cánovas, A.; Hansen, S.; Otero-Díaz, L. Electron Microscopy Study of Tubular Crystals $(BiS)_{1+d}(NbS_2)_n$. *Micron* **2000**, *31*, 587–595.
15. Radovsky, G.; Popovitz-Biro, R.; Staiger, M.; Gartsman, K.; Thomsen, C.; Lorenz, T.; Seifert, G.; Tenne, R. Synthesis of Copious Amounts of SnS_2 and SnS_2/SnS Nanotubes With Ordered Superstructures. *Angew. Chem., Int. Ed.* **2011**, *50*, 12316–12320.
16. Panchakarla, L. S.; Radovsky, G.; Houben, L.; Popovitz-Biro, R.; Dunin-Borkowski, R. E.; Tenne, R. Nanotubes From Misfit Layered Compounds: A New Family of Materials With Low Dimensionality. *J. Phys. Chem. Lett.* **2014**, *5*, 3724–3736.
17. Wang, Y.; Suna, A.; Mahler, W.; Kasowski, R. PbS in Polymers. From Molecules to Bulk Solids. *J. Chem. Phys.* **1987**, *87*, 7315–7322.
18. Thangaraju, B.; Kaliannan, P. Spray Pyrolytic Deposition and Characterization of SnS and SnS_2 Thin Films. *J. Phys. D: Appl. Phys.* **2000**, *33*, 1054–1059.
19. Lorenz, T.; Joswig, J.-O.; Seifert, G. Combined SnS@SnS_2 Double Layers: Charge Transfer and Electronic Structure. *Semicond. Sci. Technol.* **2014**, *29*, 064006.
20. Lorenz, T.; Joswig, J.-O.; Seifert, G. Two-Dimensional and Tubular Structures of Misfit Compounds: Structural and Electronic Properties. *Beilstein J. Nanotechnol.* **2014**, *5*, 2171–2178.
21. Ren, Y.; Haas, C.; Wiegers, G. A. Photoelectron Spectroscopy Study of the Electronic Structure of the Incommensurate Intergrowth Compounds $(SbS)_{1.15}(TiS_2)_n$ With n = 1,2. *J. Phys.: Condens. Matter* **1995**, *7*, 5949–5958.
22. Noda, Y.; Ohba, S.; Sato, S.; Saito, Y. Charge Distribution and Atomic Thermal Vibration in Lead Chalcogenide Crystals. *Acta Crystallogr., Sect. B: Struct. Sci.* **1983**, *39*, 312–317.
23. Margolin, A.; Popovitz-Biro, R.; Albu-Yaron, A.; Rapoport, L.; Tenne, R. Fullerene-Like Nanoparticles of Titanium Disulfide. *Chem. Phys. Lett.* **2005**, *411*, 162–166.
24. Feldman, Y.; Frey, G.; Homyonfer, M.; Lyakhovitskaya, V.; Margulis, L.; Cohen, H.; Hodes, G.; Hutchison, J.; Tenne, R. Bulk Synthesis of Inorganic Fullerene-like MS_2 (M=Mo,W) from the Respective Trioxides and the Reaction Mechanism. *J. Am. Chem. Soc.* **1996**, *118*, 5362–5367.
25. Ordejón, P.; Artacho, E.; Soler, J. M. Self-Consistent Order-*N* Density-Functional Calculations For Very Large Systems. *Phys. Rev. B: Condens. Matter Mater. Phys.* **1996**, *53*, R10441–R10444.
26. Soler, J. M.; Artacho, E.; Gale, J. D.; Garcia, A.; Junquera, J.; Ordejón, P.; Sánchez-Portal, D. The SIESTA Method For *Ab Initio* Order-*N* Materials Simulation. *J. Phys.: Condens. Matter* **2002**, *14*, 2745–2779.
27. Hohenberg, P.; Kohn, W. Inhomogeneous Electron Gas. *Phys. Rev.* **1964**, *136*, B864–B871.
28. Perdew, J. P.; Burke, K.; Ernzerhof, M. Generalized Gradient Approximation Made Simple. *Phys. Rev. Lett.* **1996**, *77*, 3865–3868.
29. Troullier, N.; Martins, J. L. Efficient Pseudopotentials For Plane-Wave Calculations. *Phys. Rev. B: Condens. Matter Mater. Phys.* **1991**, *43*, 1993–2006.
30. Moreno, J.; Soler, J. M. Optimal Meshes For Integrals in Real- and Reciprocal-Space Unit Cells. *Phys. Rev. B: Condens. Matter Mater. Phys.* **1992**, *45*, 13891–13898.
31. Monkhorst, H. J.; Pack, J. D. Special Points For Brillouin-Zone Integrations. *Phys. Rev. B* **1976**, *13*, 5188–5192.
32. Zhang, L.; Song, Q.; Zhang, S. B. Exceptionally Strong Hydrogen Bonds Affect the Surface Energy of Colloidal Nanocrystals: Methylamine and Water Adsoprtion on PbS. *Phys. Rev. Lett.* **2010**, *104*, 116101.
33. Björkman, T.; Gulans, A.; Krasheninnikov, A. V.; Nieminen, R. M. Van Der Waals Bonding in Layered Compounds From Advanced Density-Functional First-Principles Calculations. *Phys. Rev. Lett.* **2012**, *108*, 235502.
34. Nanda, K. K.; Maisels, A.; Kruis, F. E.; Fissan, H.; Stappert, S. Higher Surface Energy of Free Nanoparticles. *Phys. Rev. Lett.* **2003**, *91*, 106102.
35. Enyashin, A.; Gemming, S.; Seifert, G. Nanosized Allotropes of Molybdenum Disulfide. *Eur. Phys. J.: Spec. Top.* **2007**, *149*, 103–125.
36. Brontvein, O.; Stroppa, D. G.; Popovitz-Biro, R.; Albu-Yaron, A.; Levy, M.; Feuerman, D.; Houben, L.; Tenne, R.; Gordon, J. M. New High-Temperature Pb-Catalyzed Synthesis of Inorganic Nanotubes. *J. Am. Chem. Soc.* **2012**, *134*, 16379–16386.